



Where's the Dust?: The Deepening Anomaly of Microwave Emission in NGC 4725 B

E. J. Murphy¹, B. S. Hensley^{2,9}, S. T. Linden³, B. T. Draine⁴, D. Dong⁵, E. Momjian⁶, G. Helou⁷, and A. S. Evans^{1,8}

¹National Radio Astronomy Observatory, 520 Edgemont Road, Charlottesville, VA 22903, USA; emurphy@nrao.edu

²Department of Astrophysical Sciences, Princeton University, Princeton, NJ 08544, USA

³Department of Astronomy, University of Virginia, 530 McCormick Road, Charlottesville, VA 22904, USA

⁴Department of Astrophysical Sciences, Princeton University, Princeton, NJ 08544, USA

⁵California Institute of Technology, MC 100-22, Pasadena, CA 91125, USA

⁶National Radio Astronomy Observatory, P.O. Box O, 1003 Lopezville Road, Socorro, NM 87801, USA

⁷Infrared Processing and Analysis Center, California Institute of Technology, MC 220-6, Pasadena CA, 91125, USA

⁸Department of Astronomy, University of Virginia, 3530 McCormick Road, Charlottesville, VA 22904, USA

Received 2020 October 12; revised 2020 November 3; accepted 2020 November 5; published 2020 December 17

Abstract

We present new Atacama Large Millimeter Array (ALMA) observations toward NGC 4725 B, a discrete, compact, optically faint region within the star-forming disk of the nearby galaxy NGC 4725 that exhibits strong anomalous microwave emission (AME). These new ALMA data include continuum observations centered at 92, 133, 203, and 221 GHz accompanied by spectral observations of the ^{12}CO ($J = 2 \rightarrow 1$) line. NGC 4725 B is detected in the continuum at all frequencies, although the detection at 203 GHz is marginal. While molecular gas is not detected at the exact location of NGC 4725 B, there is molecular gas in the immediate vicinity (i.e., $\lesssim 100$ pc) along with associated diffuse $8\ \mu\text{m}$ emission. When combined with existing Very Large Array continuum data at 1.5, 3, 5.5, 9, 14, 22, 33, and 44 GHz, the spectrum is best fit by a combination of AME, synchrotron, and free-free emission that is free-free absorbed below ~ 6 GHz. Given the strength of the AME, there is surprisingly no indication of millimeter dust emission associated with NGC 4725 B on $\lesssim 6''$ spatial scales at the sensitivity of the ALMA interferometric data. Based on the properties of the nearest molecular gas complex and the inferred star formation rate, NGC 4725 B is consistent with being an extremely young ($\sim 3\text{--}5$ Myr) massive ($\lesssim 10^5 M_{\odot}$) cluster that is undergoing active cluster feedback. However, the lack of millimeter thermal dust emission is difficult to reconcile with a spinning dust origin of the 30 GHz emission. On the other hand, modeling NGC 4725 B as a new class of background radio galaxy is also unsatisfactory.

Unified Astronomy Thesaurus concepts: [Radio continuum emission \(1340\)](#); [Interstellar emissions \(840\)](#); [Dust continuum emission \(412\)](#); [H II regions \(694\)](#); [Star forming regions \(1565\)](#); [Star formation \(1569\)](#); [Galaxies \(573\)](#); [Disk galaxies \(391\)](#)

1. Introduction

It has been over 20 yr since the initial discovery of excess ~ 30 GHz (~ 1 cm), dust-correlated emission in cosmic microwave background experiments (e.g., Kogut et al. 1996; Leitch et al. 1997), yet our current understanding of the physical mechanism and environmental conditions powering anomalous microwave emission (AME) remains highly incomplete (for a recent review, see Dickinson et al. (2018)). The leading explanation for AME is “spinning dust,” in which rapidly rotating ultrasmall (radius $a \lesssim 1$ nm) grains with a nonzero electric dipole moment produce a peaked microwave emission spectrum in the frequency range spanning $\approx 10\text{--}60$ GHz (Erickson 1957; Draine & Lazarian 1998; Ali-Haïmoud et al. 2009; Hoang et al. 2011; Hensley & Draine 2017).

To date, AME has been observed in a wide variety of astrophysical environments, indicating that it is truly a ubiquitous emission component in the interstellar medium (ISM) of galaxies, and that a complete model may significantly impact our understanding of the astrophysics of the ISM. For instance, investigations within the Galaxy have uncovered strong detections of AME in molecular clouds (e.g., Planck Collaboration et al. 2011) along with discrete locations adjacent to larger H II complexes (e.g., Dickinson et al. 2009; Tibbs et al. 2011), consistent with the theoretical expectation that it is a common emission component in galaxies. Most recently, detection of AME has been reported in

protoplanetary disks around Herbig Ae stars (Greaves et al. 2018). Although seemingly a common phenomenon from Galactic sources, AME has been observed in surprisingly few extragalactic sources, with only NGC 6946 (Murphy et al. 2010; Scaife et al. 2010; Hensley et al. 2015), NGC 4725 (Murphy et al. 2018c), and M31 (Battistelli et al. 2019) having firm detections. This dearth of extragalactic detections likely arises from the lack of deep, wide-field observations of nearby extragalactic sources at ~ 30 GHz, the insensitivity of interferometers to large angular scale emission, and the need for multifrequency data (Hensley et al. 2015; Linden et al. 2020).

In this Letter, we revisit the recent detection of AME from an optically faint region within the star-forming galaxy NGC 4725 from 33 GHz Karl G. Jansky Very Large Array (VLA) observations carried out as part of the Star Formation in Radio Survey (SFRS; Murphy et al. 2018b; Linden et al. 2020). This source, NGC 4725 B, was studied by Murphy et al. (2018c), who concluded that it was consistent with a highly embedded ($A_V > 5$ mag) nascent star-forming region, in which young ($\lesssim 3$ Myr) massive stars are still enshrouded by their natal cocoons of gas and dust, lacking enough supernovae to produce measurable synchrotron emission. In light of our new Atacama Large Millimeter Array (ALMA) continuum and molecular gas observations of NGC 4725 B, along with additional archival VLA data, this scenario remains largely viable. However, the ALMA data raise a new and unexpected question regarding the origin of the AME—how can such a strong

⁹ Spitzer Fellow.

Table 1
Observational Data

Freq. (GHz)	Synthesized Beam	σ ($\mu\text{Jy bm}^{-1}$)	σ_{T_b} (mK)	S_*^a (μJy)
1.50	1''32 × 1''09	31.1	11697.0	<106.0
3.00	1''85 × 1''76	13.7	569.37	157.0 ± 14.0
5.50	0''36 × 0''31	12.2	4387.4	299.0 ± 19.0
9.00	0''25 × 0''21	10.8	3125.6	248.0 ± 22.0
14.0	0''15 × 0''12	10.1	3478.4	210.0 ± 19.0
22.0	1''50 × 0''89	20.5	38.340	297.0 ± 23.0
33.0	0''91 × 0''58	21.4	45.310	359.0 ± 31.0
44.0	0''63 × 0''50	32.9	66.700	214.0 ± 51.0
92.0	0''54 × 0''37	8.88	7.4800	139.0 ± 15.0
133.0	0''48 × 0''29	14.8	8.1000	106.0 ± 33.0
203.0	0''69 × 0''40	17.2	1.9800	53.7 ± 32.0
221.0	0''51 × 0''34	13.4	1.8000	84.3 ± 28.0
$^{12}\text{CO} (J = 2 \rightarrow 1)$ Emission Line				
		($\text{Jy bm}^{-1} \text{ km s}^{-1}$)	(K km s^{-1})	(Jy km s^{-1})
229.6	0''61 × 0''46	0.038	3.15	<0.820

Note.

^a Photometry measured after convolving all data to match the synthesized beam of the 3 GHz data.

30 GHz excess be produced without an accompanying millimeter dust continuum?

This Letter is organized as follows: The data and analysis procedures are presented in Section 2. The results are then presented in Section 3. Finally we provide a brief discussion of our findings and our main conclusions in Section 4.

2. Data and Analysis

We refer the reader to Murphy et al. (2018c) for detailed information on NGC 4725 and NGC 4725 B, along with the associated data and analysis procedures presented in that paper. In this Letter, we simply summarize key details of that work and present the new ALMA and archival VLA data, as well as associated analysis procedures, and discuss how these new data affect the previous interpretation.

NGC 4725 is a nearby ($d_L = 11.9$ Mpc; Freedman et al. 2001) barred ringed spiral galaxy that hosts an active galactic nucleus (Sy2) nucleus (Moustakas et al. 2010). Located at J2000 $\alpha = 12^{\text{h}}50^{\text{m}}28^{\text{s}}.48$, $\delta = +25^{\circ}30'22''.5$ (at a galactocentric radius of ≈ 1.9 kpc), NGC 4725 B was first detected at 33 GHz as part of SFRS Murphy et al. (2018b), comprising nuclear and extranuclear star-forming regions in 56 nearby galaxies ($d_L < 30$ Mpc) observed as part of the Spitzer Infrared Nearby Galaxies Survey (SINGS; Kennicutt et al. 2003) and Key Insights on Nearby Galaxies: a Far-Infrared Survey with Herschel (KINGFISH; Kennicutt et al. 2011) legacy programs.

2.1. VLA Data Reduction and Imaging

Radio data were obtained as part of multiple campaigns using the VLA covering the S- (2–4 GHz), Ku- (12–18 GHz), K- (18–26.5 GHz), Ka- (26.5–40 GHz), and Q- (40–50 GHz) bands, which are summarized in Table 1. Details on the data reduction and imaging procedures can be found in Murphy et al. (2018b, 2018c) and Linden et al. (2020). To summarize, we followed standard calibration procedures, using the VLA calibration pipeline built on the Common Astronomy Software

Applications (CASA; McMullin et al. 2007) versions 4.6.0 and 4.7.0. After each initial pipeline run, we manually inspected the calibration tables and visibilities for signs of instrumental problems (e.g., bad deformatters) and RFI, flagging them correspondingly. After flagging, we reran the pipeline, and we repeated this process until we could not detect any further signs of bad data.

As with the data calibration, a detailed description of the imaging procedure used here can be found in Murphy et al. (2018b) and Linden et al. (2020). To summarize, calibrated VLA measurement sets for each source were imaged using the task TCLEAN in CASA version 4.7.0. The synthesized beam, point-source rms, and surface brightness rms for each final image are given in Table 1. Employing the ALMA Cycle 4 handbook definition of the largest angular scale (LAS), we find the LAS to which these images are sensitive to be $\theta_{\text{LAS}} \approx 31''.5$, $23''.5$, $16''.9$, $11''.3$, and $8''.44$ at 3, 15, 22, 33, and 44 GHz, respectively, where the calculations have been done with the CASA Analysis Utilities task ESTIMATEMRS.

We additionally make use of archival VLA data (VLA/12B-191) that included observations toward the nucleus of NGC 4725 in the L- (1–2 GHz), C- (4–8 GHz), X (8–12), and Ku-bands. These data were taken in the A-configuration and made use of the 8 bit samplers. The L-band data had a maximum instantaneous bandwidth of 1 GHz with a central frequency of 1.5 GHz. The data of the remaining frequency bands had a maximum of 2 GHz of bandwidth with central frequencies of 5.5, 9, and 14 GHz for the C-, X-, and Ku-band imaging, respectively. These data were reduced using the VLA calibration pipeline built on CASA version 5.3.0. The synthesized beam, point-source rms, and surface brightness rms for each final image are given in Table 1. Again, using the task ESTIMATEMRS, the LAS that these images are sensitive to are $\theta_{\text{LAS}} \approx 19''.2$, $5''.26$, $3''.19$, and $2''.05$ at 1.5, 5.5, 9, and 14 GHz, respectively.

Calibrated data were imaged using the task TCLEAN in CASA version 5.6.1. The mode of TCLEAN was set to multifrequency synthesis (MFS; Conway et al. 1990; Sault & Wieringa 1994). We chose to use *Briggs* weighting with ROBUST = 0.5. Given that the fractional bandwidth is $>10\%$ for each band, we set the variable NTERMS = 2, which allows the cleaning procedure to also model the spectral index variations on the sky. For the L-band imaging, we additionally made use of the W-projection algorithm to help deal with bright sources far from the phase center. Unlike the 14 GHz data, the 15 GHz data delivered a nonoptimal calibration, which was evident in the data of the phase calibrator source itself. The resulting 14 GHz image created from these archival data is therefore used exclusively in the present analysis.

2.2. ALMA Data Reduction and Imaging

ALMA data were obtained during Cycle 6 (Project Code: 2018.1.01826.S) in Bands 3, 4, 5, and 6, and are summarized in Table 1. Observations at Bands 3, 4, and 5 were centered at 92, 133, and 203 GHz, respectively, for dedicated continuum imaging; observations at each band used four spectral windows with a bandwidth of 1.875 GHz and 31.250 MHz spectral channels. For Band 6 observations, three spectral windows were set up for dedicated continuum imaging similar to Bands 3, 4, and 5 observations. However, the fourth spectral window was tuned to 229.612 GHz with a bandwidth of 1.875 GHz and spectral resolution of 1938.477 kHz (2.531 km s^{-1}) to detect $^{12}\text{CO} (J = 2 \rightarrow 1)$ at a rest frequency of 230.5424 GHz. The

corresponding continuum image created from the line-free Band 6 data is centered at 221 GHz.

Like the VLA data, the ALMA data were reduced and calibrated using CASA following standard procedures as part of the ALMA quality assurance process. The ALMA data were reduced using both the ALMA calibration pipeline with CASA version 5.4.0, as well as prepared manual reduction and imaging scripts. Calibrated data were imaged using the task TCLEAN in CASA version 5.6.1. The mode of TCLEAN was set to multifrequency synthesis (MFS; Conway et al. 1990; Sault & Wieringa 1994). We chose to use *Briggs* weighting with ROBUST = 0.5. For Bands 3 and 4, where the fractional bandwidth was >10%, we set the variable NTERMS = 2, which allows the cleaning procedure to also model the spectral index variations on the sky. For continuum imaging of Bands 5 and 6, we instead set the variable NTERMS = 1; in the case of Band 6, we imaged the three dedicated continuum spectral windows and the line-free portion of the fourth spectral window. In all cases of the continuum imaging, we do not make use of the multiscale clean option (Cornwell 2008; Rau & Cornwell 2011). The synthesized beam, point-source rms, and surface brightness rms for each final image are given in Table 1. Based on the task ESTIMATEMRS, the LAS to which these images are sensitive are $\theta_{\text{LAS}} \approx 6''.64$, $5''.10$, $5''.76$, and $4''.76$ at 92, 133, 203, and 221 GHz respectively. In Figure 1, $15'' \times 15''$ ($\approx 900 \text{ pc} \times 900 \text{ pc}$) cutouts centered on the location of NGC 4725 B are shown for all radio and millimeter data.

Similar to the continuum imaging, the $J = 2 \rightarrow 1$ CO line data were imaged using TCLEAN, but instead setting the mode to “cube.” Unlike the ALMA continuum emission for NGC 4725 B, the molecular gas appears extended (see Figure 2). Consequently, we also made use of the multiscale clean option (Cornwell 2008; Rau & Cornwell 2011) to help deconvolve extended low-intensity line emission and to search for structures with scales ≈ 1 and 3 times the FWHM of the synthesized beam. The moment 0 map was then created by integrating the spectral cube at each pixel limited to the portion of velocity space associated with line emission. The synthesized beam and rms of the $J = 2 \rightarrow 1$ CO moment 0 map are given in Table 1. The $J = 2 \rightarrow 1$ CO moment 0 contours are overlaid on each radio and millimeter continuum image in Figure 1.

2.3. Photometry

Photometry was carried out at all frequencies before applying a primary beam correction. To measure the flux densities of the source at each frequency, we first beam-match the data to the lowest-resolution beam among all images (i.e., the 3 GHz data) using the CASA task IMSMOOTH. We elect to exclude the much lower-resolution 2013 March 33 GHz data included in Murphy et al. (2018c), because they are significantly (i.e., a factor of ~ 30) coarser than the ALMA data (i.e., $2''.89 \times 1''.97$); convolving the data to such a low angular resolution typically reduces/removes the statistical significance of a detection in the higher-frequency ALMA bands. Further, we make use of the archival VLA 14 GHz data only, rather than the newer 15 GHz data, due to the much better calibration and imaging quality of the final map.

Next, the CASA task IMFIT was used to fit an elliptical Gaussian to the emission within a circular aperture having a radius equal to the FWHM of the synthesized beam major axis of the beam matched images (i.e., $1''.85$). Given the proximity of NGC 4725 B to the phase center of each observation,

primary beam corrections were negligible (i.e., $<1\%$) at all frequencies except 5.5, 9, and 14 GHz, where correction factors of 1.011, 1.032, 1.079 were applied to the reported peak brightnesses and integrated flux densities (along with their errors), respectively. These factors were obtained via the frequency-dependent primary beam correction given in EVLA Memo# 195 (Perley 2016).¹⁰

The source is unresolved in all of the native-resolution images using the criterion that the fitted major axis ϕ_M be at least $2\sigma_{\phi_M}$ larger than the FWHM of the synthesized beam major axis. Similarly, the source appears unresolved in the beam-matched images at all frequencies. Consequently, we take the total flux density (S_*) for the unresolved cases to be the geometric mean of the peak brightness and integrated flux density reported by IMFIT. We choose this value because it provides the most accurate measurement for the flux density of a weak source, given that the uncertainties on the peak brightness and integrated flux density from the elliptical Gaussian fitting are anticorrelated (Condon 1997).

The total flux densities, along with their uncertainties, are given in Table 1 at each frequency. While IMFIT formally reported a statistically significant detection at 1.5 GHz (i.e., $S_* = 134 \pm 30$), it is clear from that map (see Figure 1) that there is nothing cospatial with NGC 4725 B and that a nearby noise feature is being fit. Consequently, we consider this as a nondetection, report the 3σ rms upper limit in Table 1, and exclude this data point from fits. There are no significant (i.e., signal-to-noise ratio > 3) detections in the beam-matched 203 GHz continuum image nor in the $J = 2 \rightarrow 1$ CO line toward NGC 4725 B. For the 203 GHz continuum, we report the IMFIT results in Table 1, as the fitting function converged and there does appear to be a source at the location of NGC 4725 B in the image. For the $J = 2 \rightarrow 1$ CO line, IMFIT failed to converge, so we therefore report the 3σ rms upper limit in Table 1. The radio-to-millimeter spectrum of NGC 4725 B is shown in Figure 3.

We note that, in Murphy et al. (2018c), they report the integrated 15 GHz flux density as S_* because the source was found to be marginally resolved (i.e., 2.3σ significance) after convolving all VLA images to the much lower resolution of their 2013 March 33 GHz. Even with differing resolutions and treatment of the source as resolved rather than unresolved, their 15 GHz flux density is consistent with the 14 GHz flux density reported in the present study.

3. Results

In the following section, we combine the new ALMA continuum and molecular gas imaging with the existing VLA continuum imaging for NGC 4725 B and perform a parametric fit to the data.

3.1. Parametric Models of the Radio-to-millimeter Spectrum

We employ a simple parametric model to fit the NGC 4725 B spectrum presented in Figure 3. The first component in the model is free-free emission, which has flux density

$$S_\nu^{\text{ff}} = B_\nu(T_e)(1 - e^{-\tau_\nu^{\text{ff}}})\pi\left(\frac{D}{2d_L}\right)^2, \quad (1)$$

¹⁰ http://library.nrao.edu/public/memos/evla/EVLAM_195.pdf

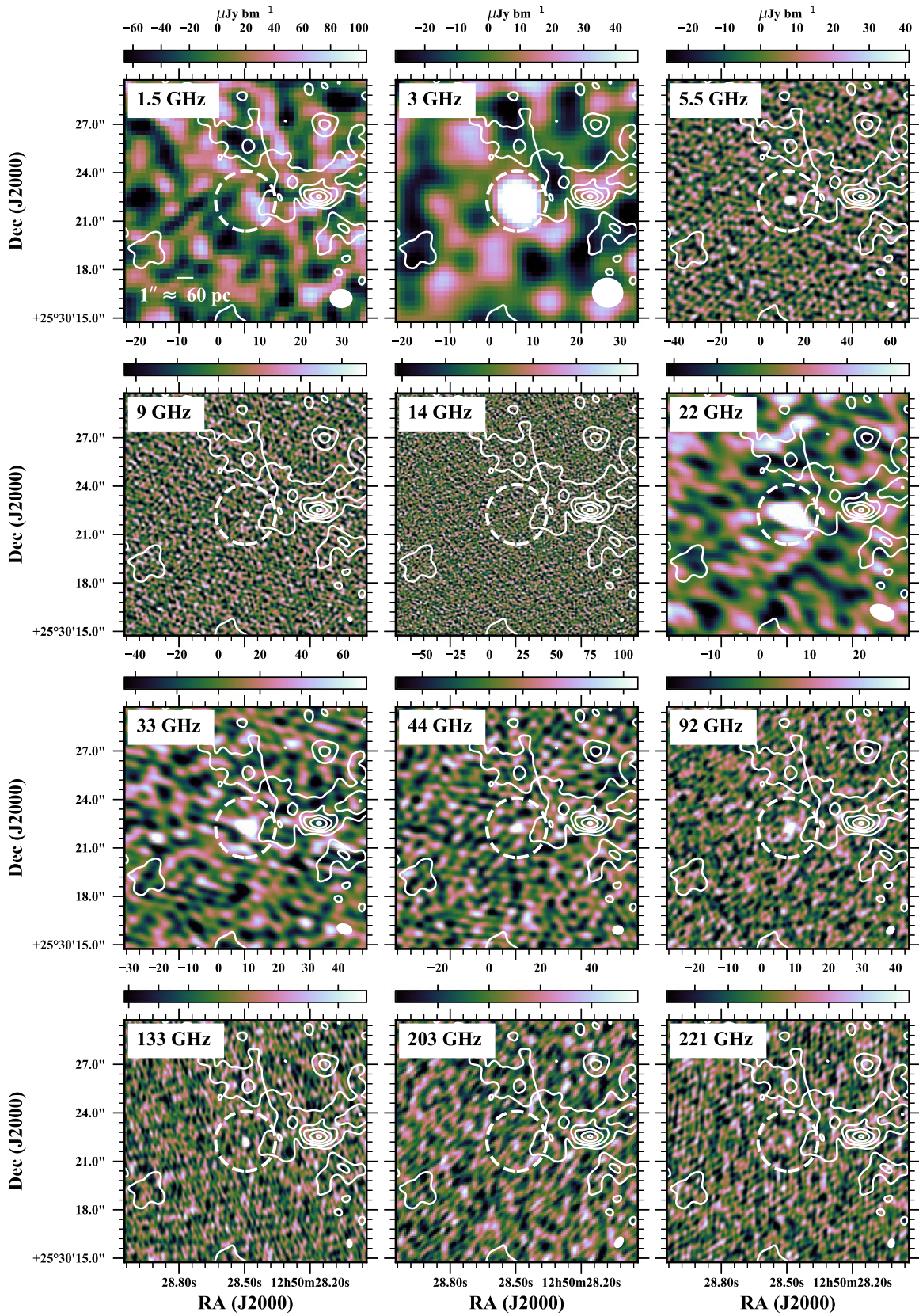


Figure 1. Color scale images displayed with a linear scaling at all observed radio/millimeter frequencies (i.e., 1.5, 3, 5.5, 9, 14, 22, 33, 44, 92, 133, 203, and 221 GHz) at their native resolutions, indicating that NGC 4725 B is detected in all bands except at 1.5 GHz. However, the detection is somewhat marginal at 203 GHz (ALMA Band 5), being $\approx 3.1\sigma$. Color bars are given in units of $\mu\text{Jy bm}^{-1}$ along the top of each panel. Overlaid on each panel are the $J=2 \rightarrow 1$ CO moment 0 contours starting at the 1σ ($=0.038 \text{ Jy bm}^{-1} \text{ km s}^{-1}$) rms level, increasing in increments of 2σ . Each panel is $15'' \times 15''$ ($\approx 900 \text{ pc} \times 900 \text{ pc}$), which is illustrated in Figure 2. The circle is centered on the source in each panel, and has a diameter of $3''7$ ($\approx 200 \text{ pc}$), which was used for the elliptical Gaussian fitting photometry. The size and orientation of the synthesized beams are illustrated in the bottom right corner of each panel. A scale bar is shown in the bottom left corner of the first panel.

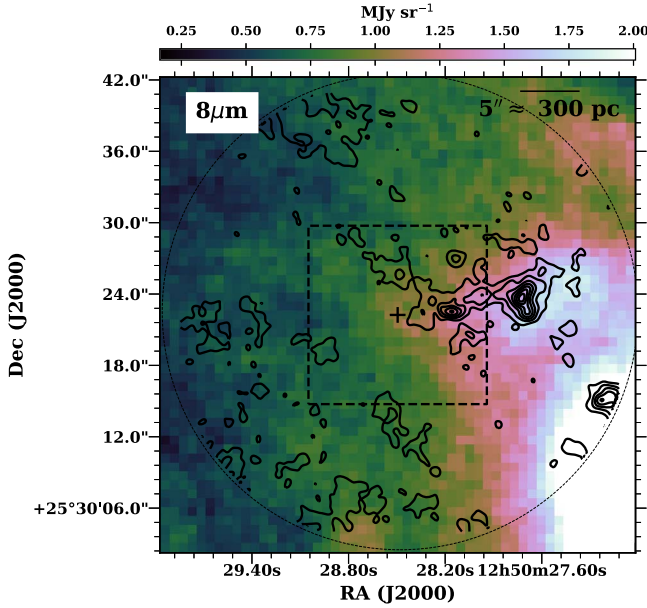


Figure 2. Spitzer/IRAC $8\ \mu\text{m}$ color scale image of NGC 4725 ($\approx 2''$ resolution) observed as part of SINGS (Kennicutt et al. 2003). Color bar is given in units of MJy sr^{-1} along the top of the figure. The $J = 2 \rightarrow 1$ CO moment 0 contours (at their native resolution) are overlaid starting at the $1\sigma (=0.038\ \text{Jy bm}^{-1}\ \text{km s}^{-1})$ rms level, increasing in increments of 2σ , and illustrating the full extent of our CO imaging; the 20% level of the primary beam response function is shown as a dashed circle. The dashed $15'' \times 15''$ box indicates the size of the panels shown in Figure 1, while the “+” symbol indicates the location of NGC 4725 B. A scale bar is shown at the top right of the image.

where T_e is the electron temperature, $B_\nu(T)$ is the Planck function, D is the diameter of the emitting region, $d_L = 11.9\ \text{Mpc}$ is the distance to NGC 4725, and τ_ν^{ff} is the free–free optical depth. We model the frequency dependence of τ_ν^{ff} in the low-frequency limit ($h\nu \ll kT_e$) following Draine (2011):

$$\tau_\nu^{\text{ff}} = \frac{4}{3} \left(\frac{2\pi}{3} \right)^{1/2} \frac{q_e^6 g_{\text{ff}} \text{EM}}{(m_e k T_e)^{3/2} c \nu^2}, \quad (2)$$

where q_e , m_e , k , and c are, respectively, the electron charge (note Gaussian units), electron mass, Boltzmann constant, and speed of light, and EM is the emission measure. We approximate the Gaunt factor g_{ff} as an analytic function of frequency and electron temperature following Draine (2011):

$$g_{\text{ff}}(\nu, T_e) = \ln \left\{ \exp \left[5.960 - \frac{\sqrt{3}}{\pi} \ln(\nu_9 T_4^{-3/2}) \right] + e \right\}, \quad (3)$$

where $\nu_9 \equiv \nu/10^9\ \text{Hz}$ and $T_4 \equiv T_e/10^4\ \text{K}$. Given the limited number of data points and the relative insensitivity of the spectrum to T_e , we fix $T_e = 10^4\ \text{K}$. It should be noted, however, that the fit value of D is sensitive to our choice of T_e , with higher assumed T_e resulting in smaller fit D and vice versa.

The spectral slope between 5 and 15 GHz suggests the presence of an optically thin synchrotron component, while the sharp decline in emission toward lower frequencies is indicative of free–free absorption. We model the optically thin synchrotron emission as a power law and the absorption as pure free–free absorption, yielding a spectrum

$$S_\nu^{\text{sync}} = A_s \left(\frac{\nu}{20\ \text{GHz}} \right)^\alpha e^{-\tau_\nu^{\text{ff}}}, \quad (4)$$

where A_s is the 20 GHz flux density in the optically thin limit. We find that the synchrotron component dominates the emission only over a narrow range of frequencies, providing little constraining power on the spectral index. We therefore adopt $\alpha = -0.83$, consistent with similar observations for star-forming galaxies (e.g., Niklas et al. 1997; Murphy et al. 2011).

While the AME component could in principle be modeled using the detailed physical prescription implemented in the `SpDust` software (Ali-Haïmoud et al. 2009; Silsbee et al. 2011), we pursue instead a simple functional description. Cepeda-Arroita et al. (2020) found that the canonical spinning dust spectra in the representative Galactic environments defined by Draine & Lazarian (1998) were well-described by

$$S_\nu^{\text{AME}} = A_{\text{AME}} \exp \left\{ -\frac{1}{2} \left[\frac{\ln(\nu/\nu_p)}{W_{\text{AME}}} \right]^2 - \tau_\nu^{\text{ff}} \right\}, \quad (5)$$

in general agreement with the more detailed parameterization derived by Stevenson (2014). Note that, for completeness, we have included a free–free absorption term, even though the effects are small at frequencies where the AME dominates. Here, ν_p is the peak frequency, A_{AME} is the flux density at ν_p , and W_{AME} governs the width of the spectrum. Cepeda-Arroita et al. (2020) found that both the theoretical spectra generated by `SpDust` and the radio observations of $\lambda\ \text{Ori}$ yielded W_{AME} in the range of 0.4–0.7. We caution that this function provides a convenient representation of the spinning dust spectrum near its peak, but is unlikely to accurately represent the low- or high-frequency tails.

Finally, the high-frequency thermal dust emission is parameterized by a modified blackbody, i.e.,

$$S_\nu^d = A_d \left(\frac{\nu}{353\ \text{GHz}} \right)^\beta \frac{B_\nu(T_d) e^{-\tau_\nu^{\text{ff}}}}{B_{353\ \text{GHz}}(T_d)}, \quad (6)$$

where A_d is the flux density at 353 GHz, T_d is the dust temperature, and $B_\nu(T)$ is the Planck function. Given the lack of high-frequency data at the requisite angular resolution and the apparent lack of strong signal in the $\nu > 100\ \text{GHz}$ data, we fix $\beta = 1.55$ and $T_d = 19.6\ \text{K}$, which are representative values for dust emission in the Galaxy (Planck Collaboration Int. XXII 2015; Planck Collaboration XI 2020). As with AME, the free–free absorption term is added only for completeness and has little effect on the spectrum at millimeter wavelengths.

3.2. Model Fits

To fit the model described in the previous section to the observed flux densities, we employ the `emcee` Markov Chain Monte Carlo software (Foreman-Mackey et al. 2013) to sample seven parameters: EM, D , A_s , A_{AME} , W_{AME} , ν_p , and A_d . We use broad, uninformative priors, requiring only that EM, D , A_s , A_{AME} , and A_d be positive, that $10 < \nu_p/\text{GHz} < 50$, and that $0 < W_{\text{AME}} < 1$.

The full seven-parameter fit yields bimodal posteriors corresponding to two distinct scenarios, which we illustrate in Figure 3. In the first scenario (Figure 3, left panel), the millimeter dust emission is consistent with zero and the AME is sharply peaked near 30 GHz. In the second scenario (Figure 3, right panel), thermal dust and free–free emission contribute roughly equally to the emission in the ALMA bands, the AME component is significantly broader and shifted to higher

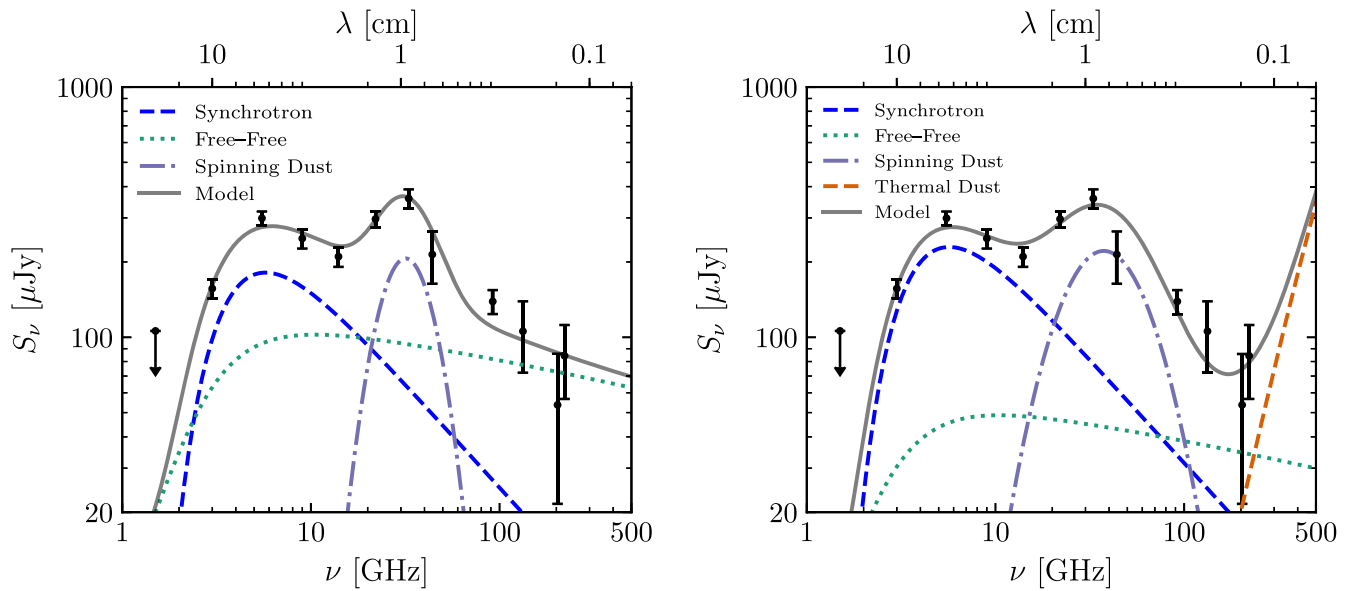


Figure 3. Radio-to-millimeter spectrum of NGC 4725 B, displaying a strong peak at ≈ 30 GHz along with two best-fit models. The model in the left panel includes free-free, spinning dust, and synchrotron emission. Free-free becomes optically thick at 3.7 GHz. In the right panel, we add millimeter dust emission as a modified blackbody with a temperature of 19.6 K and $\beta = 1.55$. Both fits provide an adequate description of the data. However, the addition of the dust component results in bimodal posteriors corresponding to the two panels here (i.e., with and without millimeter dust emission). In both fits, we find that the free-free emission is consistent with a region having $EM \approx 1.4 \times 10^{26} \text{ cm}^{-5}$ and physical size $D \approx 2$ pc.

frequencies ($\nu_p = 38$ GHz), and the synchrotron emission dominates the low-frequency spectrum. The model without millimeter dust emission is the maximum likelihood solution, and so we consider this our default model and quote parameter constraints from a six-parameter fit fixing $A_d = 0$. Inclusion of a small amount of dust emission does not qualitatively alter this fit and cannot be ruled out; this model should be considered as representative of the scenario in which emission in the ALMA bands is mostly free-free. As we discuss in greater detail in Section 4.1.3, the alternate scenario with significant thermal dust emission at millimeter wavelengths does not modify our principal conclusions, including the fact that the millimeter emission is much weaker than anticipated if the 30 GHz excess is attributed to spinning dust. The full posterior distributions are presented in Figure 4.

Despite the simplicity of the model with no millimeter dust emission (i.e., $A_d = 0$), it provides an excellent description of the data ($\chi^2 = 9.0$ for a six-parameter fit to eleven data points). To match the turnover at low frequencies, free-free absorption is required. We find that the free-free emission can be explained by a region with $EM = (1.46 \pm 0.15) \times 10^{26} \text{ cm}^{-5}$ and physical size $D = 2.30^{+0.30}_{-0.49}$ pc. The free-free optical depth is unity at 3.7 GHz. In general agreement with the analysis of Murphy et al. (2018c), we find that free-free accounts for only 25% of the 30 GHz emission, with AME dominating at this frequency. We differ in our analysis by the inclusion of synchrotron emission, which contributes 18% of the 30 GHz emission in this model. The 30 GHz excess is fit well with an AME component described by Equation (5) and having a peak frequency of $\nu_p = 31.6^{+6.5}_{-3.0}$ GHz and a rather narrow width of $W_{AME} = 0.32^{+0.20}_{-0.11}$. For completeness, the remaining model parameters have fit values of $A_s = 95^{+21}_{-17} \mu\text{Jy}$ and $A_{AME} = 209^{+47}_{-37} \mu\text{Jy}$.

The greatest discrepancy between the data and the model is at 92 GHz, where the model is 1.9σ too low, but this may also be an indication that the simple functional form used to fit the

AME component (Equation (5)) falls off too rapidly at high frequencies. More observations are needed to better constrain the shape of the spectrum, particularly at frequencies above 30 GHz.

The alternative solution with nonzero millimeter dust emission differs significantly in the relative importance of the emission mechanisms. The observed 30 GHz emission is accounted for by $202 \mu\text{Jy}$ of AME (62% of the total), $87 \mu\text{Jy}$ of synchrotron (27%), and only $37 \mu\text{Jy}$ of free-free (11%) in this model. The greatly reduced free-free emission allows for the incorporation of dust emission at higher frequencies. In this scenario, the millimeter dust continuum and free-free emission contribute equally at 228 GHz. The 95% upper limit on dust emission at 353 GHz is $167 \mu\text{Jy}$. The AME component is much broader ($W_{AME} = 0.5$) and the peak frequency is shifted to 38 GHz. However, the quality of the fit is poorer even with the addition of the extra fitting parameter ($\chi^2 = 10.3$ fitting seven parameters to eleven data points). On the other hand, it would be surprising for NGC 4725B to lack millimeter dust emission entirely.

3.3. Associated Molecular Gas: ^{12}CO ($J = 2 \rightarrow 1$)

In Figure 2, the $J = 2 \rightarrow 1$ CO moment 0 contours are plotted on a Spitzer/IRAC $8 \mu\text{m}$ color scale image extending out to the 20% level of the primary beam response, indicating a significant amount of molecular gas present in this vicinity of the star-forming disk. This is consistent with expectations based on existing lower-resolution (i.e., $\theta_{1/2} \approx 13''.4$) $J = 2 \rightarrow 1$ CO data (Leroy et al. 2009). The molecular gas distribution loosely follows the $8 \mu\text{m}$ brightness, which is a tracer of small dust grains and polycyclic aromatic hydrocarbons (PAHs). Figure 1 shows a zoom-in of the $J = 2 \rightarrow 1$ CO moment 0 contours overlaid on each of the radio and millimeter color scale images.

The fact that the CO ($J = 2 \rightarrow 1$) does not peak exactly at the location of continuum emission from NGC 4725 B on $\lesssim 100$ pc

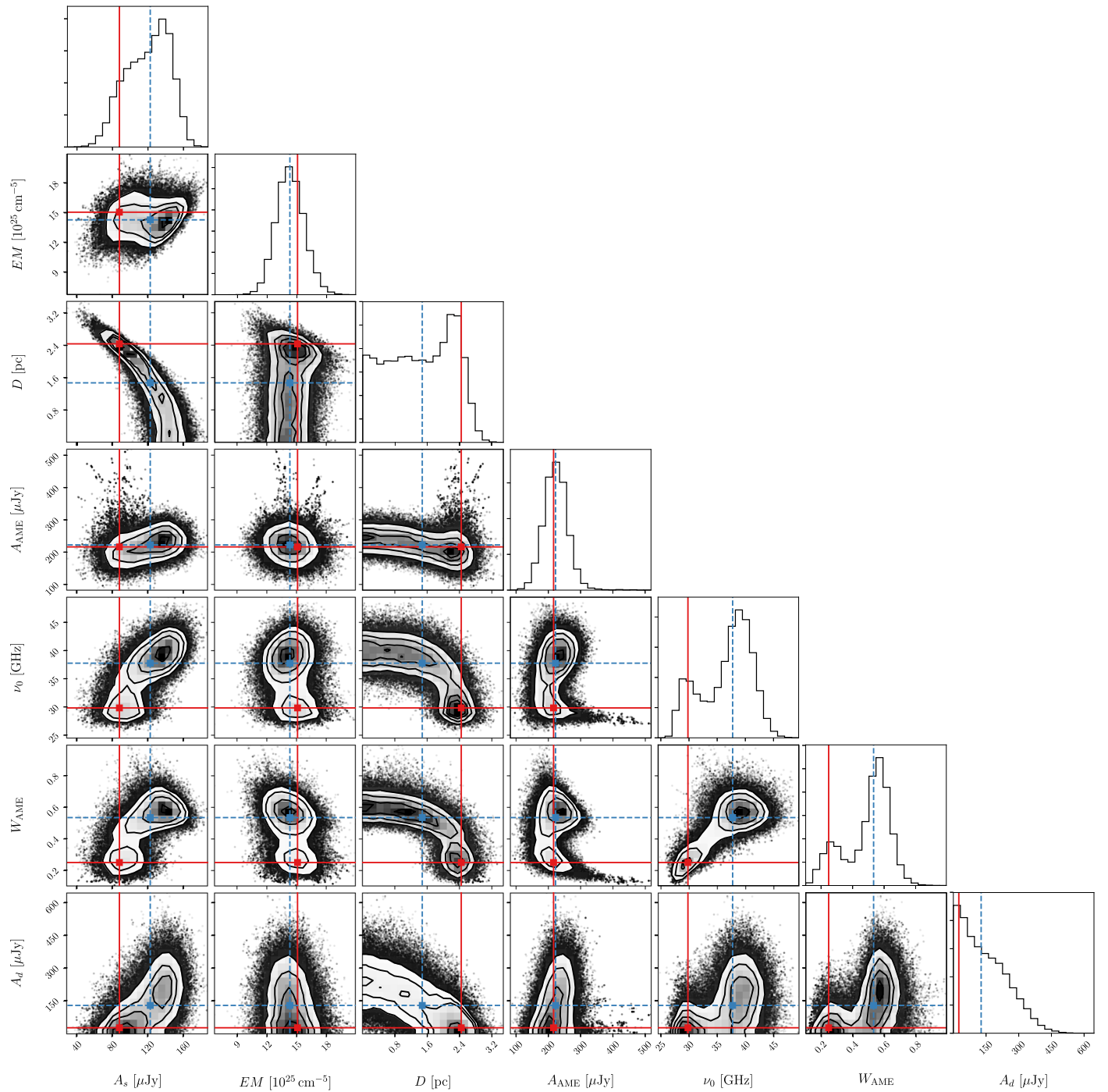


Figure 4. Posterior distributions for all seven fit parameters of the model described in Section 3.1. Maximum likelihood values are indicated with red solid line and correspond to the solution with no millimeter dust emission (i.e., $A_d = 0$). Posterior medians are indicated with blue dashed lines and correspond roughly to the other local maximum in the posterior distributions.

scales is not surprising (e.g., Murphy et al. 2015) given that the molecular gas has already been converted into stars, with plenty of additional gas nearby available for future star formation. The integrated line luminosity of the nearest CO feature ≈ 260 pc to the west of NGC 4725 B is $L'_{\text{CO}} \approx (2.2 \pm 0.23) \times 10^5 \text{ K km s}^{-1} \text{ pc}^2$. Assuming both a CO ($J = 2 \rightarrow 1$)/CO ($J = 1 \rightarrow 0$) brightness temperature ratio of ~ 0.8 (e.g., Leroy et al. 2009; Zschaechner et al. 2018) and $\alpha_{\text{CO}} \approx 4.3 M_{\odot} (\text{K km s}^{-1} \text{ pc}^2)^{-1}$ (e.g., Solomon & Vanden Bout 2005; Bolatto et al. 2013), the total nearby molecular gas reservoir is measured to be $M_{\text{H}_2} \gtrsim 1.2 \times 10^6 M_{\odot}$. For comparison, given the 3σ upper

limit of $\lesssim 7.1 \times 10^4 \text{ K km s}^{-1} \text{ pc}^2$ at the location of NGC 4725 B, the corresponding upper limit on the molecular gas mass is $M_{\text{H}_2} \lesssim 3.8 \times 10^5 M_{\odot}$.

4. Discussion and Conclusions

We discuss here the possible origins of the emission observed from NGC 4725 B, including spinning dust emission in a massive cluster and synchrotron emission in a background radio source. Neither provides a completely satisfactory explanation of the spectrum and the apparent compactness.

4.1. A Forming Massive Cluster?

4.1.1. Cluster Properties

The new ALMA data presented in this study appear consistent with the conclusion of Murphy et al. (2018c) that NGC 4725 B is a nascent star-forming region, where massive stars are still highly enshrouded by their natal cocoons of gas and dust. The archival VLA data suggest the presence of synchrotron emission in addition to a significant amount of free-free emission, and thus an age of $\sim 3\text{--}5$ Myr. Assuming that $\approx 50\%$ of the 14 GHz flux density arises from free-free emission, based on the best-fit model in the left panel of Figure 3, suggests an ionizing photon rate of $Q(H^0) \approx 1.4 \times 10^{51} \text{ s}^{-1}$ (Murphy et al. 2011, Equation (10)), or ≈ 125 O7V stars, where $Q(H^0) \approx 10^{49} \text{ s}^{-1}$ per $37.7 M_{\odot}$ O7V star (Sternberg et al. 2003). Using a Kroupa initial mass function (Kroupa 2001) fully populated between 0.1 and $100 M_{\odot}$ implies a total stellar mass of $M_{\star} \approx 6.4 \times 10^4 M_{\odot}$ for NGC 4725 B. It is worth stressing that our results and conclusions remain qualitatively the same even if we were to instead use the best-fit model in the right panel of Figure 3. In that case, the fraction of free-free emission at 14 GHz reduces to $\approx 20\%$ of the total flux density, which in turn reduces the associated ionizing photon rate and stellar mass estimate by $\approx 40\%$ (i.e., $Q(H^0) \approx 5.9 \times 10^{50} \text{ s}^{-1}$ and $M_{\star} \approx 2.6 \times 10^4 M_{\odot}$).

With a stellar mass of $\lesssim 10^5 M_{\odot}$ located in a ~ 2 pc region, NGC 4725 B is best defined as a young massive star cluster (YMC; Portegies Zwart et al. 2010). In that context, we find that the mass NGC 4725 B is consistent with the upper end of star cluster masses derived for other nearby galaxies (e.g., NGC 628 and M51) as part of the Legacy Extragalactic UV Survey (LEGUS; Calzetti et al. 2015). Further, the estimated cluster radius of ~ 1 pc agrees with observations of the youngest YMCs studied in the LEGUS sample (Ryon et al. 2017). Finally, radial gradients in the maximum cluster mass have been observed for several nearby spiral galaxies, such that clusters with $M_{\star} \gtrsim 10^4 M_{\odot}$ are found predominantly within the central ~ 2 kpc (Adamo et al. 2017; Messa et al. 2018). This is consistent with NGC 4725 B, which is located at ~ 1.9 kpc from the nucleus of NGC 4725.

Using a combination of ALMA, HST, and VLA observations of the Antennae Galaxies, Whitmore et al. (2014) developed a classification system for YMCs such that the presence and strength of different multiwavelength tracers of star formation activity can be used as an independent metric to age date star clusters. With bright and compact radio emission, a large inferred value for the dust attenuation, and the presence of nearby diffuse/faint CO (see Section 4.1.2), NGC 4725 B is classified as a stage 3 “emerging cluster,” which places an upper limit on the inferred cluster age of $\lesssim 3\text{--}5$ Myr. This is consistent with the age inferred from the radio emission alone.

During this phase of cluster evolution, the natal gas and dust surrounding the cluster are actively removed via feedback from stellar winds and UV radiation (Lada & Lada 2003). In this context, the lack of CO gas and millimeter dust emission observed is perhaps not that surprising or unexpected. Furthermore, while there is not a significant detection at the exact location of NGC 4725 B, the molecular gas appears to be in the immediate vicinity of NGC 4725 B (i.e., $\lesssim 100$ pc) and could have fueled the nascent star formation in NGC 4725 B. Assuming an age of ~ 5 Myr for the star formation and a distance of ~ 100 pc to the nearby molecular gas reservoir suggests an asymmetric drift

velocity of $\sim 20 \text{ km s}^{-1}$ between NGC 4725 B and the CO gas, which seems completely plausible (e.g., Quirk et al. 2019).

Miura et al. (2012) used CO observations of M33 to classify giant molecular clouds (GMCs) into different evolutionary stages. Given the number of O7V stars estimated above, NGC 4725 B and the associated GMC would be classified as a stage “C” star-forming region with an age of $\sim 3\text{--}5$ Myr and a mean CO ($J = 2 \rightarrow 1$) flux of $L'_{\text{CO}} \sim 7.2 \times 10^4 \text{ K km s}^{-1} \text{ pc}^2$ with an associated standard deviation of $\sigma_{L'_{\text{CO}}} \sim 4.6 \times 10^4 \text{ K km s}^{-1} \text{ pc}^2$. Given the large dispersion, this value is consistent with our nondetection (i.e., $L'_{\text{CO}} \lesssim 7.1 \times 10^4 \text{ K km s}^{-1} \text{ pc}^2$) at the location of NGC 4725 B.

4.1.2. Molecular Gas Properties

Let us assume that NGC 4725 B formed from a cloud of similar mass in the nearby molecular gas reservoir to the west (i.e., $M_{\text{H}_2} \approx 1.2 \times 10^6 M_{\odot}$; see Section 3.3). Using Murphy et al. (2011, Equation (1)), we convert the value of $Q(H^0)$ given above to a star formation rate of $0.010 M_{\odot} \text{ yr}^{-1}$ for NGC 4725 B. This implies a gas depletion time of $t_{\text{dep}} \gtrsim 113$ Myr. The gas depletion time inferred here is a factor of ≈ 4 shorter than that for starburst galaxies in the Great Observatories All-Sky LIRG Survey (GOALS; Armus et al. 2009; Herrero-Illana et al. 2019) and a factor of ≈ 16 shorter than that derived for resolved measurements on 60–120 pc scales for normal star-forming galaxies included in the Physics at High Angular Resolution in nearby Galaxies (PHANGS)-ALMA sample (Utomo et al. 2018).

Assuming a constant 100 pc thickness of the molecular gas layer for this CO complex suggests a gravitational freefall time of $t_{\text{ff}} \sim 6$ Myr and a star formation efficiency per gravitational freefall time of $\epsilon_{\text{ff}} \sim 5\%$. The inferred values of τ_{ff} and ϵ_{ff} for the CO feature near NGC 4725 B are a factor of ≈ 2 shorter and a factor of ≈ 8 larger than the corresponding average values reported for the PHANGS-ALMA sample (Utomo et al. 2018), respectively, suggesting relatively efficient star formation. This high star formation efficiency per gravitational freefall time is further supported by taking the ratio of estimated stellar mass in NGC 4725 B to the nearby total molecular gas mass, which implies that $\lesssim 5\%$ of the gas has recently been converted into stars.

Simulations of turbulent, magnetized star-forming clouds (i.e., with a mass of $\sim 10^5 M_{\odot}$) that include stellar radiation and outflow feedback predict a full range of ϵ_{ff} spanning $\lesssim 1\%$ – 100% . In these simulations, ϵ_{ff} is small at low densities. As mass flows rapidly into higher-density regions within the cloud, ϵ_{ff} approaches unity (Khullar et al. 2019) with little time spent at intermediate densities. Therefore, the ϵ_{ff} derived for NGC 4725 B may suggest that this object is being observed in a short-lived phase of its evolution.

In this context, it may not be unexpected that the AME signatures in this region are unique relative to the AME seen in our Galaxy. The Galaxy contains no YMCs with masses $\gtrsim 10^5 M_{\odot}$, and if these particular properties of the AME are indeed associated with a short-lived period of massive cluster evolution, we would not expect to observe such interstellar medium conditions in our Galaxy.

4.1.3. Physical Constraints on AME

Surprisingly, even with the addition of ALMA data at 92, 133, 203, and 221 GHz, there is no evidence for high-frequency thermal dust emission at these sensitivities. As discussed in

Section 3.1, we derive an upper limit (95% confidence) on the 353 GHz flux density from dust emission of $167 \mu\text{Jy}$. To place this limit in context, we note that the Galaxy has a typical ratio of 30 GHz AME specific intensity to 353 GHz optical depth τ_{353} of 200 MJy sr^{-1} , whether in the diffuse interstellar medium or in cloud complexes like Perseus (Hensley et al. 2016; Dickinson et al. 2018). For an assumed dust temperature of 20 K and $1''.85$ beam, our fit suggests $\tau_{353} < 4 \times 10^{-5}$. Combining this with a peak AME flux density of $208 \mu\text{Jy}$ yields a ratio of $6 \times 10^4 \text{ MJy sr}^{-1}$, roughly 300 times larger than typically seen in the Galaxy. The maximum likelihood solution (left panel of Figure 3) invokes no dust emission at all, greatly exacerbating this discrepancy.

Given the surprising lack of millimeter dust emission inferred from the full model fit, we quantify the maximum permitted by the ALMA data without accounting for other emission mechanisms. Fitting just the 203 and 221 GHz ALMA observations with the modified blackbody dust model, we derive a 95% upper limit of $520 \mu\text{Jy}$ at 353 GHz. Even in this maximally conservative scenario, the ratio of AME to millimeter dust emission exceeds Galactic values by a factor of 100.

4.1.4. Lack of Millimeter Dust Continuum

Emission from ~ 20 K grains is almost certainly present in the region, based on much coarser far-infrared data; however, it may be present only on much larger spatial scales that are invisible to the ALMA interferometric observations (i.e., $\gtrsim 6''$). For instance, there is clearly widespread diffuse Spitzer/IRAC $8 \mu\text{m}$ emission all around the vicinity of NGC 4725 B (see Figure 2), indicating the presence of small dust grains and PAHs. As was shown in Murphy et al. (2018c, Figure 3), there appear to be counterparts at the location of NGC 4725 B detected in IRAC maps both at 3.6 and $4.5 \mu\text{m}$, indicating the presence of small/hot dust grains that could be powering the observed AME.

We measure a $3.6 \mu\text{m}$ flux density of $974 \mu\text{Jy}$ integrating in a $2''.4$ aperture and applying an aperture correction factor of 1.215 as given in Table 4.7 of the IRAC instrument handbook. In the $3.5 \mu\text{m}$ DIRBE band, Dwek et al. (1997) measured a typical dust emission per H-atom of $1.18 \times 10^{-23} \text{ MJy sr}^{-1} \text{ H}^{-1}$, while Planck Collaboration Int. XVII (2014) measured a value of $6.7 \times 10^{-24} \text{ MJy sr}^{-1} \text{ H}^{-1}$ at 100 GHz. If this ratio of mid-infrared to millimeter emission holds for NGC 4725 B, we would expect $550 \mu\text{Jy}$ of dust emission at 100 GHz, well in excess of the total observed emission ($\sim 130 \mu\text{Jy}$). The differing resolutions of the Spitzer and ALMA data and the imperfect correspondence between the IRAC and DIRBE bandpasses may account for some of this discrepancy. However, it is likely that the radiation field is stronger in NGC 4725B than on a typical diffuse Galactic sightline. A factor of ~ 5 difference in the ratio of PAH to submillimeter emission could be accommodated by a factor of ~ 5 difference in the strength of the intensity of starlight heating the grains. Thus, the lack of submillimeter continuum at the current sensitivity limits is not implausible, given the observed PAH emission in the vicinity of this region.

NGC 4725B lacks not only dust continuum detectable at these sensitivities, but also any appreciable CO emission. In Section 3.3, we found that the upper limit on ^{12}CO ($J = 2 \rightarrow 1$) implies $M_{\text{H}_2} \lesssim 3.8 \times 10^5 M_{\odot}$. At 230 GHz, the Draine & Li (2007) dust model emits $2.1 \times 10^{-27} \text{ erg s}^{-1} \text{ H}^{-1}$ when illuminated by starlight characteristic of the diffuse Galactic ISM. Using this

emissivity, $4 \times 10^5 M_{\odot}$ of gas at a distance of 11.9 Mpc corresponds to only $26 \mu\text{Jy}$ of continuum emission at 230 GHz. Thus, the upper limit on the gas mass implied by the nondetection of CO is completely consistent with the lack of observed dust emission.

On the basis of these arguments, the lack of millimeter dust continuum is completely consistent with the observed synchrotron, free-free, CO, and PAH emission in NGC 4725 B, supporting the interpretation that this object is a massive cluster within the galaxy disk. However, this scenario does not readily explain the peaked 30 GHz emission. If it is attributed to spinning dust grains, then the millimeter dust continuum should be roughly two orders of magnitude brighter than observed.

4.2. A Background Source?

The compact nature of NGC 4725 and extreme ratio of 30 GHz AME relative to 353 GHz dust emission are clearly at odds with expectations from spinning dust emission. However, as discussed in Murphy et al. (2018c), attributing NGC 4725 B to a chance background galaxy is also problematic, though it cannot be completely ruled out. First, there are no known submillijansky radio sources that peak at such high frequencies. Furthermore, while the submillijansky extragalactic sky at $\gtrsim 30$ GHz is not well-known, naively extrapolating from existing number counts (e.g., Massardi et al. 2011; Murphy & Chary 2018) suggests that finding a source with a rising spectrum between 5 and 20 GHz given the SFRS survey area is unlikely (i.e., $< 17\%$, Murphy et al. 2018c). This is a conservative upper limit, given that this estimate both assumes uniform noise in the SFRS survey area and uses the full sample of Massardi et al. (2011), which also finds that the fraction of sources with rising spectra decreases with decreasing flux density. For example, applying an average primary beam correction to the SFRS noise and extrapolating from the fraction of sources with rising spectra between 5 and 20 GHz in their lowest flux density bin (i.e., $40 \leq S_{20 \text{ GHz}} < 100 \text{ mJy}$, which is still more than $100\times$ brighter than NGC 4725 B) decreases the likelihood of finding such a source to $< 10\%$. Assuming this trend continues, it would then suggest an even lower likelihood of finding such a source, given the 22 GHz flux density of NGC 4725 B (i.e., $S_{22 \text{ GHz}} \approx 300 \mu\text{Jy}$).

The spectrum of NGC 4725 B also seems much too sharply peaked to be explained by a ‘‘classical’’ (synchrotron self-absorbed) gigahertz-peaked spectrum (GPS) radio galaxy (Condon & Ransom 2016). Furthermore, if the source were a GPS source at redshift $z \approx 1$ with a turnover frequency of 31.6 GHz (i.e., 63.2 GHz in the source frame) and a corresponding flux density of $\sim 365 \mu\text{Jy}$, the empirical turnover-size relation given by Orienti & Dallacasa (2014) suggests a physical diameter of $D \approx 0.4 \text{ pc}$. This would then imply an internal magnetic field strength of $\sim 6 \times 10^5 \text{ G}$ (Condon & Ransom 2016), which is extraordinarily large. Assuming a spherical source, the corresponding magnetic energy ($E_B = U_B V$, where $U_B = B^2/(8\pi)$ is the magnetic energy density and V is the source volume) would be $\sim 1.1 \times 10^{64} \text{ erg}$, exceeding the gravitational binding energy ($E_G \approx 2GM^2/D$) unless the enclosed mass were $M > 1.6 \times 10^{11} M_{\odot}$! While this empirical turnover-size relation was derived for sources with typical flux densities as large as $\sim 100 \text{ mJy}$ (i.e., $\sim 300\times$ larger than NGC 4725 B), by locating it at $z \approx 1$, its rest-frame 5 GHz spectral luminosity would be consistent with the low-luminosity end of the core emission in that sample (i.e.,

$L_{5\text{ GHz}} \sim 1.1 \times 10^{24} \text{ W Hz}^{-1}$). Thus, such a scenario seems implausible.

Although it remains possible that NGC 4725 B is a new class of compact, optically faint, ~ 30 GHz peaking radio galaxy, on the basis of these arguments it still seems most likely that it is located in the disk of NGC 4725. Future high-resolution (i.e., $\lesssim 0''.01$) radio imaging may be able to discriminate between these scenarios.

4.3. Final Thoughts

While the expectation was that these new ALMA data would help definitively characterize the physical conditions of NGC 4725 B and explain why there is such a strong presence of AME, they have in fact raised further questions. It is extraordinary that NGC 4725 B has strongly peaked emission at ≈ 1 cm without any detectable dust emission at millimeter wavelengths.

If the excess 30 GHz emission is being produced by spinning ultrasmall grains, the extreme ratio of 30 GHz AME relative to 353 GHz dust emission suggests, at minimum, substantial differences in the small grain population in this region with respect to those in Galactic AME regions. Models of Galactic dust that reproduce both far-infrared emission and AME require at least $\sim 5\%$ of the dust mass to reside in grains $\lesssim 1$ nm in size (Draine & Lazarian 1998; Hoang et al. 2016; Hensley & Draine 2017). Thus, a factor of ~ 300 enhancement in the 30 GHz emissivity relative to diffuse Galactic sightlines could not be achieved even if 100% of the dust mass were in nanoparticles. Other factors would be required, such as grains having much larger typical electric dipole moments while maintaining comparable rotation frequencies. Another possibility might be a scenario in which all of the grains were reduced to a sufficiently small size ($\lesssim 5$ nm) as not to emit efficiently at long wavelengths. While not completely implausible, these considerations cast doubt on a spinning dust origin of the 30 GHz emission.

Alternatively, an emission mechanism such as thermal magnetic dipole emission (Draine & Lazarian 1999; Draine & Hensley 2013) might produce elevated 30 GHz relative to 353 GHz emission through systematic changes in the physical properties of the grains. However, such an explanation would require significant fine-tuning of the dust optical properties and aspect ratios to achieve such strong ferromagnetic resonance behavior, and we thus consider it unlikely.

At this point, it seems that more observations are required to make further progress on determining the true physical nature of this source and why there appears to be such strong AME. For instance, significantly deeper, high angular resolution VLA/VLBA and ALMA data should help to better constrain the spectrum (e.g., determine if the ALMA measurements are completely dominated by pure free-free emission) and angular extent of NGC 4725 B. Looking toward the future, next-generation ground- and space-based facilities should contribute substantially to such studies. A next-generation VLA (ngVLA; Murphy et al. 2018a; McKinnon et al. 2019), delivering an order-of-magnitude improvement in sensitivity and angular resolution over the existing VLA, will be highly optimized for studying faint sources like NGC 4725 B at frequencies spanning ~ 1.2 – 116 GHz. While future far-infrared measurements at a high enough angular resolution to constrain the total infrared emission from NGC 4725 B will need to wait a decade or more for a space-based telescope, such as the currently conceived Origins Space Telescope, observing the 3.3 and 3.4 μm hydrocarbon features

with the Near-Infrared Spectrograph on board the James Webb Space Telescope could help shed critically needed light on potential AME carriers.

We would like to thank the anonymous referee for comments that helped to improve the content and presentation of this Letter. E. J. M. thanks J. J. Condon for useful discussions that helped improve the paper. The National Radio Astronomy Observatory is a facility of the National Science Foundation operated under cooperative agreement by Associated Universities, Inc. This paper makes use of the following ALMA data: ADS/JAO.ALMA#2018.1.01826.S. ALMA is a partnership of ESO (representing its member states), NSF (USA), and NINS (Japan), together with NRC (Canada), MOST and ASIAA (Taiwan), and KASI (Republic of Korea), in cooperation with the Republic of Chile. The Joint ALMA Observatory is operated by ESO, AUI/NRAO, and NAOJ.

Software: APLpy (Robitaille & Bressert 2012; Robitaille 2019), CASA (v4.6.0, v4.7.0, v5.3.0, v5.4.0, v5.6.1 McMullin et al. 2007), corner (Foreman-Mackey 2016), emcee (Foreman-Mackey et al. 2013), Matplotlib (Hunter 2007), NumPy (van der Walt et al. 2011).

ORCID iDs

E. J. Murphy  <https://orcid.org/0000-0001-7089-7325>
 B. S. Hensley  <https://orcid.org/0000-0001-7449-4638>
 S. T. Linden  <https://orcid.org/0000-0002-1000-6081>
 B. T. Draine  <https://orcid.org/0000-0002-0846-936X>
 E. Momjian  <https://orcid.org/0000-0003-3168-5922>
 G. Helou  <https://orcid.org/0000-0003-3367-3415>

References

- Adamo, A., Ryon, J. E., Messa, M., et al. 2017, *ApJ*, 841, 131
 Ali-Haïmoud, Y., Hirata, C. M., & Dickinson, C. 2009, *MNRAS*, 395, 1055
 Armus, L., Mazzarella, J. M., Evans, A. S., et al. 2009, *PASP*, 121, 559
 Battistelli, E. S., Fatigoni, S., Murgia, M., et al. 2019, *ApJL*, 877, L31
 Bolatto, A. D., Wolfire, M., & Leroy, A. K. 2013, *ARA&A*, 51, 207
 Calzetti, D., Lee, J. C., Sabbi, E., et al. 2015, *AJ*, 149, 51
 Cepeda-Arroita, R., Harper, S., Dickinson, C., et al. 2020, arXiv:2001.07159
 Condon, J. J. 1997, *PASP*, 109, 166
 Condon, J. J., & Ransom, S. M. 2016, *Essential Radio Astronomy* (Princeton, NJ: Princeton Univ. Press)
 Conway, J. E., Cornwell, T. J., & Wilkinson, P. N. 1990, *MNRAS*, 246, 490
 Cornwell, T. J. 2008, *ISTSP*, 2, 793
 Dickinson, C., Ali-Haïmoud, Y., Barr, A., et al. 2018, *NewAR*, 80, 1
 Dickinson, C., Davies, R. D., Allison, J. R., et al. 2009, *ApJ*, 690, 1585
 Draine, B. T. 2011, *Physics of the Interstellar and Intergalactic Medium* (Princeton, NJ: Princeton Univ. Press)
 Draine, B. T., & Hensley, B. 2013, *ApJ*, 765, 159
 Draine, B. T., & Lazarian, A. 1998, *ApJ*, 508, 157
 Draine, B. T., & Lazarian, A. 1999, *ApJ*, 512, 740
 Draine, B. T., & Li, A. 2007, *ApJ*, 657, 810
 Dwek, E., Arendt, R. G., Fixsen, D. J., et al. 1997, *ApJ*, 475, 565
 Erickson, W. C. 1957, *ApJ*, 126, 480
 Foreman-Mackey, D. 2016, *JOSS*, 1, 24
 Foreman-Mackey, D., Hogg, D. W., Lang, D., & Goodman, J. 2013, *PASP*, 125, 306
 Freedman, W. L., Madore, B. F., Gibson, B. K., et al. 2001, *ApJ*, 553, 47
 Greaves, J. S., Scaife, A. M. M., Frayer, D. T., et al. 2018, *NatAs*, 2, 662
 Hensley, B., Murphy, E., & Staguhn, J. 2015, *MNRAS*, 449, 809
 Hensley, B. S., & Draine, B. T. 2017, *ApJ*, 836, 179
 Hensley, B. S., Draine, B. T., & Meisner, A. M. 2016, *ApJ*, 827, 45
 Herrero-Illana, R., Privon, G. C., Evans, A. S., et al. 2019, *A&A*, 628, A71
 Hoang, T., Lazarian, A., & Draine, B. T. 2011, *ApJ*, 741, 87
 Hoang, T., Vinh, N.-A., & Quynh Lan, N. 2016, *ApJ*, 824, 18
 Hunter, J. D. 2007, *CSE*, 9, 90
 Kennicutt, R. C., Calzetti, D., Aniano, G., et al. 2011, *PASP*, 123, 1347
 Kennicutt, R. C., Jr., Armus, L., Bendo, G., et al. 2003, *PASP*, 115, 928

- Khullar, S., Krumholz, M. R., Federrath, C., & Cunningham, A. J. 2019, *MNRAS*, **488**, 1407
- Kogut, A., Banday, A. J., Bennett, C. L., et al. 1996, *ApJL*, **464**, L5
- Kroupa, P. 2001, *MNRAS*, **322**, 231
- Lada, C. J., & Lada, E. A. 2003, *ARA&A*, **41**, 57
- Leitch, E. M., Readhead, A. C. S., Pearson, T. J., & Myers, S. T. 1997, *ApJL*, **486**, L23
- Leroy, A. K., Walter, F., Bigiel, F., et al. 2009, *AJ*, **137**, 4670
- Linden, S. T., Murphy, E. J., Dong, D., et al. 2020, *ApJS*, **248**, 25
- Massardi, M., Ekers, R. D., Murphy, T., et al. 2011, *MNRAS*, **412**, 318
- McKinnon, M., Beasley, A., Murphy, E., et al. 2019, *BAAS*, **51**, 81
- McMullin, J. P., Waters, B., Schiebel, D., Young, W., & Golap, K. 2007, in *ASP Conf. Ser. 376, Astronomical Data Analysis Software and Systems XVI*, ed. R. A. Shaw, F. Hill, & D. J. Bell (San Francisco, CA: ASP), 127
- Messa, M., Adamo, A., Calzetti, D., et al. 2018, *MNRAS*, **477**, 1683
- Miura, R. E., Kohno, K., Tosaki, T., et al. 2012, *ApJ*, **761**, 37
- Moustakas, J., Kennicutt, R. C., Jr., Tremonti, C. A., et al. 2010, *ApJS*, **190**, 233
- Murphy, E. J., Bolatto, A., Chatterjee, S., et al. 2018a, in *ASP Conf. Ser. 517, Science with a Next Generation Very Large Array*, ed. E. Murphy (San Francisco, CA: ASP), 3
- Murphy, E. J., & Chary, R.-R. 2018, *ApJ*, **861**, 27
- Murphy, E. J., Condon, J. J., Schinnerer, E., et al. 2011, *ApJ*, **737**, 67
- Murphy, E. J., Dong, D., Leroy, A. K., et al. 2015, *ApJ*, **813**, 118
- Murphy, E. J., Dong, D., Momjian, E., et al. 2018b, *ApJS*, **234**, 24
- Murphy, E. J., Helou, G., Condon, J. J., et al. 2010, *ApJL*, **709**, L108
- Murphy, E. J., Linden, S. T., Dong, D., et al. 2018c, *ApJ*, **862**, 20
- Niklas, S., Klein, U., & Wielebinski, R. 1997, *A&A*, **322**, 19
- Orienti, M., & Dallacasa, D. 2014, *MNRAS*, **438**, 463
- Planck Collaboration, Ade, P. A. R., Aghanim, N., et al. 2011, *A&A*, **536**, A20
- Planck Collaboration Int. XVII 2014, *A&A*, **566**, A55
- Planck Collaboration Int. XXII 2015, *A&A*, **576**, A107
- Planck Collaboration XI 2020, *A&A*, **641**, A11
- Portegies Zwart, S. F., McMillan, S. L. W., & Gieles, M. 2010, *ARA&A*, **48**, 431
- Quirk, A., Guhathakurta, P., Chemin, L., et al. 2019, *ApJ*, **871**, 11
- Rau, U., & Cornwell, T. J. 2011, *A&A*, **532**, A71
- Robitaille, T. 2019, *APLpy v2.0: The Astronomical Plotting Library in Python*, Zenodo, doi:[10.5281/zenodo.2567476](https://doi.org/10.5281/zenodo.2567476)
- Robitaille, T., & Bressert, E. 2012, *APLpy: Astronomical Plotting Library in Python*, Astrophysics Source Code Library, ascl:[1208.017](https://ascl.net/1208.017)
- Ryon, J. E., Gallagher, J. S., Smith, L. J., et al. 2017, *ApJ*, **841**, 92
- Sault, R. J., & Wieringa, M. H. 1994, *A&AS*, **108**, 585
- Scaife, A. M. M., Nikolic, B., Green, D. A., et al. 2010, *MNRAS*, **406**, L45
- Silsbee, K., Ali-Haïmoud, Y., & Hirata, C. M. 2011, *MNRAS*, **411**, 2750
- Solomon, P. M., & Vanden Bout, P. A. 2005, *ARA&A*, **43**, 677
- Sternberg, A., Hoffmann, T. L., & Pauldrach, A. W. A. 2003, *ApJ*, **599**, 1333
- Stevenson, M. A. 2014, *ApJ*, **781**, 113
- Tibbs, C. T., Flagey, N., Paladini, R., et al. 2011, *MNRAS*, **418**, 1889
- Utomo, D., Sun, J., Leroy, A. K., et al. 2018, *ApJL*, **861**, L18
- van der Walt, S., Colbert, S. C., & Varoquaux, G. 2011, *CSE*, **13**, 22
- Whitmore, B. C., Brogan, C., Chandar, R., et al. 2014, *ApJ*, **795**, 156
- Zschaechner, L. K., Bolatto, A. D., Walter, F., et al. 2018, *ApJ*, **867**, 111